



Optical transmission spectra of ordered porous alumina membranes with different thicknesses and porosities

W.L. Xu, H. Chen, M.J. Zheng, G.Q. Ding, W.Z. Shen *

Laboratory of Condensed Matter Spectroscopy and Opto-Electronic Physics, Department of Physics,
Shanghai Jiao Tong University, 1954 Hua Shan Road, Shanghai 200030, PR China

Received 16 April 2005; accepted 12 July 2005
Available online 18 August 2005

Abstract

We employ a modified four-layer-medium transmission model to extract the thickness, wavelength-dependent refractive index, band gap and band tail of highly ordered porous alumina membranes (PAMs) anodized in oxalic acid, from visible and ultraviolet optical transmission spectra. The yielded thickness as a function of second-anodization time is in good agreement with the scanning electron microscope data, as well as the theoretical results from the current density–time characteristics. The pore widening process in phosphoric acid reveals inhomogeneous dissolution vertical to the nanopores. From the refractive index results, the nonuniform distribution of anions in the host alumina has been suggested in oxalic acid PAMs. Moreover, compared with bulk alumina, the observation of band gap reduction and band tails in PAMs is related with the electronic interband transition from the valence band to unoccupied defect states located in the band gaps, possibly originating from the oxygen vacancies (F^+ centers) and oxalic impurities in PAMs.

© 2005 Elsevier B.V. All rights reserved.

PACS: 78.67.-n; 78.20.Bh; 78.20.Ci; 81.07.-b

1. Introduction

The electrochemically produced porous alumina membranes (PAMs) with highly ordered nanopore arrays [1] have been widely used as templates for the fabrication of ordered nanostructures with nanorod or nanowire arrays of various materials [2–9], owing to their unique regular nanoscale structures and relatively easy and low-cost processing. Due to their many novel properties, these ordered nanostructures have potential applications in various fields, such as magnetic storage

[10], solar cells [11] and photonic crystals [12]. In-depth studies on the ordered porous alumina have been very necessary for the arisen new area, and detailed optical characteristics are of technological importance from the viewpoints of both the PAMs and the synthesized nanomaterials for optical device application.

The photoluminescence (PL) and Raman scattering characteristics of the PAMs have been investigated extensively [13–16]. In accordance with the previous optical study of disordered anodic alumina [17–19] for waveguide devices, the thickness and refractive index of PAMs have been the recent subjects of discussion. PL-induced Fabry–Pérot interferences have been employed to characterize *in situ* optical thickness of PAMs [20]. And Choi et al. [21] have studied the reflectivity of phosphoric acid PAMs in infrared region which was measured on a plane cleavage after the alumina

* Corresponding author. Tel.: +86 21 54743242; fax: +86 21 54741040.

E-mail addresses: mjzheng@sjtu.edu.cn (M.J. Zheng), wzshen@sjtu.edu.cn (W.Z. Shen).

structure had been broken carefully. They have suggested that the porous alumina structure is composed of a duplex oxide layer based on the yielded refractive indices of the oxide layers.

In this paper, we employ a simple and effective method to determine the thickness, wavelength-dependent refractive index, and band gap of the oxalic acid PAMs prepared under different second-anodization times and different porosities by using visible and ultraviolet transmission spectra. Based on the yielded results, we propose the inhomogeneous dissolution vertical to the nanopores during the pore widening process in phosphoric acid. The nonuniform distribution of anions in the host alumina is suggested in the oxalic acid PAMs. Furthermore, the observation of band gap reduction and band tails is related with the electronic interband transition from the valence band to unoccupied defect states located in the band gaps.

2. Experimental

The PAMs were fabricated through a typical two-step anodizing electrochemical procedure [1] with high-purity (99.999%) aluminum foil as the anode in 0.3 M $C_2H_2O_4$ electrolyte. The first anodization lasted for 4 h at the constant anodizing voltage of 40 V and electrolyte temperature of 12 °C. The specimens were then immersed in a mixture of 6.0 wt% H_3PO_4 and 1.8 wt% H_2CrO_4 at 60 °C for 6 h to remove the alumina layers. The highly ordered porous alumina was formed after the second anodization under the same conditions as the first one for 10–30 min. In order to obtain different porosities by widening the pore sizes, the PAMs were immersed in 5 wt% phosphoric acid at 30 °C for 0–30 min after the second anodization. The cross section morphology and thickness of the prepared PAMs were characterized by field-emission scanning electron microscope (FE-SEM) on Philips XL30FEG with a spatial resolution of 2 nm. Fig. 1(a) shows the SEM image of a typical PAM top part. It is clear that the PAM consists of top barrier layer and nanopore array with the barrier layer thickness, nanopore diameter and interpore spacing of ~40, 40 and 100 nm, respectively.

For the optical characterization of the porous alumina, we first remove the unoxidized aluminum in a mixed solution of saturated $CuSO_4$ and HCl, and then transfer the PAMs onto the transparent glass substrates. The optical transmission measurements were performed on a Jobin Yvon 460 monochromator for the PAMs with different thicknesses (by different second-anodization times) and porosities (by different phosphoric acid immersion times) in the wavelength range of 190–900 nm. The current density–time characteristics during the second anodization were recorded by a Keithley 2400 sourcemeter.

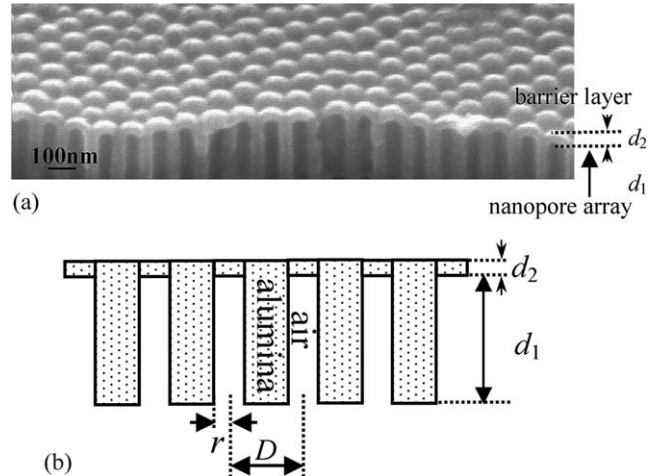


Fig. 1. (a) Cross section SEM morphology of a typical PAM top part, where top barrier layer and nanopore array can be clearly revealed. (b) Schematic of the PAM dielectric medium for the theoretical model of the optical transmission, with d_1 and d_2 for the thickness of nanopore array and top barrier layer, respectively.

3. Results and discussion

Fig. 2 shows the experimental transmission spectra (filled circles) of the as-prepared (without immersed in phosphoric acid) PAMs under different second-anodization times (T_a) from 10 to 30 min. Prominent Fabry–Pérot interference fringes due to multiple layer-substrate reflections are observed in the visible region of Fig. 2(a), and vanish in the strong ultraviolet band gap absorption

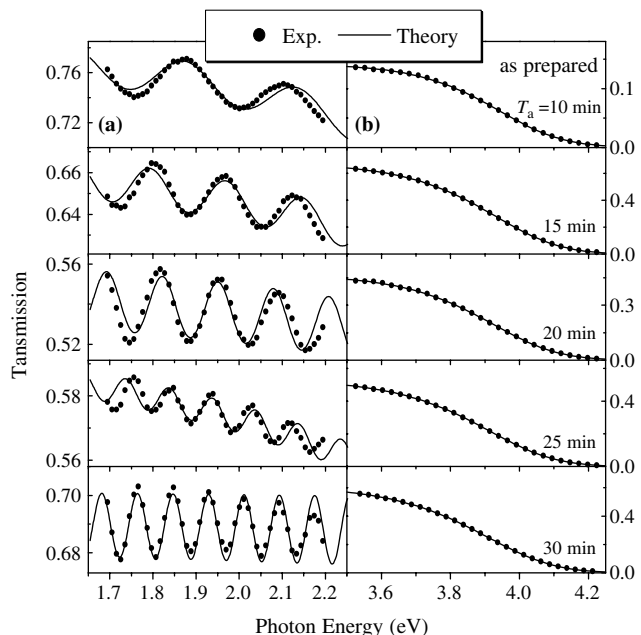


Fig. 2. Experimental (filled circles) and calculated (solid curves) transmission spectra in (a) visible and (b) ultraviolet wavelength range for as-prepared PAMs (immersion time in phosphoric acid $T_i = 0$) under different second-anodization times T_a .

region of alumina around 3.5–4.2 eV in Fig. 2(b). We can clearly observe that the number of the interference fringes increases with the second-anodization time due to the increase of PAM thickness. Fig. 3 displays the experimental transmission spectra (filled circles) of the PAMs under different immersion times (T_i) in phosphoric acid from 0 (as-prepared) to 30 min with the same second-anodization time of 30 min. We note that the change of interference fringe number occurs only in the long immersion time of 30 min.

By using the modified four-layer-medium transmission model (i.e., air/PAM/substrate/air here) and the same fitting procedure described in Ref. [22], we determine both the wavelength-dependent refractive index of the host alumina in PAMs below the band gap and the film thickness of PAMs from the observed interference fringes of optical transmission spectra. In the calculation, the optical transmission equation is

$$T_r(\lambda, d_f) = \frac{A(1-L)\exp(-\alpha d_f)}{B + C\exp(-\alpha d_f) + D\exp(-2\alpha d_f)}, \quad (1)$$

where $T_r(\lambda)$ is the magnitude of transmission, α is the absorption coefficient, d_f is the film thickness, and parameters A , B , C , D , and L are given in Ref. [22].

Nevertheless, it should be noted that, the dielectric medium is composed of alumina and air with different proportions. In order to obtain the optical properties of the host alumina, as shown schematically in Fig. 1(b), we treat the observed transmission of the PAMs as the sum of two parts of host alumina with different thicknesses (i.e., the whole PAM thickness

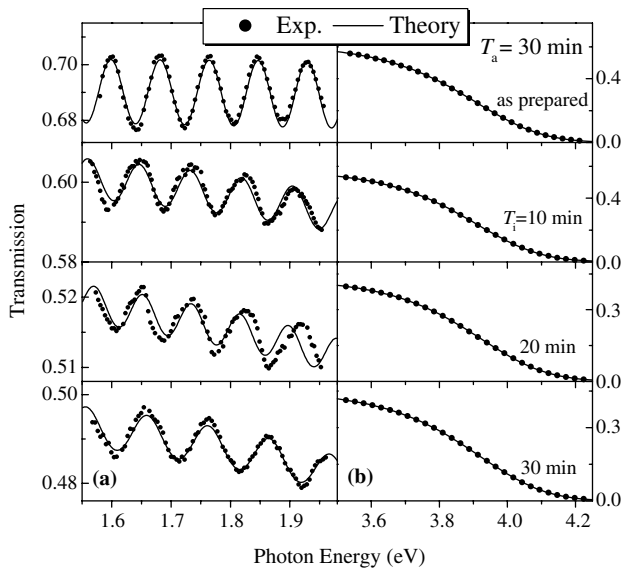


Fig. 3. Experimental (filled circles) and calculated (solid curves) transmission spectra in (a) visible and (b) ultraviolet wavelength range for PAMs under different immersion times T_i in phosphoric acid from 0 (as prepared) to 30 min with the same second-anodization time T_a of 30 min.

$d = d_1 + d_2$ and only the barrier layer thickness d_2 with the ratio of $(1-p)$ and p , respectively)

$$T_r(\lambda, d_f) = T_r(\lambda, (d_1 + d_2)) \cdot (1-p) + T_r(\lambda, d_2) \cdot p, \quad (2)$$

where p is the PAM porosity estimated through $p = 2\pi(r/D)^2/\sqrt{3}$ [23] with r the radius of the pores and D the interpore spacing. The solid curves in Figs. 2(a) and 3(a) are the theoretical interference fringes, which fit well with the experimental data.

We illustrate the yielded nanopore thickness d_1 in the as-prepared PAMs with different second-anodization times as filled circles in Fig. 4(a). In order to confirm the reliability of the transmission model for the thin film thickness, a direct comparison has been made among the optical data, the FE-SEM results and the theoretical results. It has been reported that, for thick PAMs, the theoretical thickness was proportional to the product of the current density (i) and the second-anodization time [24]. However, during the second anodization, the current density, as shown in Fig. 4(b), first experiences a rapid drop within 30 s, then increases slowly up to 2 min, and finally keeps as a constant basically with the anodization going on. Therefore, for thin PAMs, especially those with second-anodization time less than 10 min, we should take into account the large variation of the current density. As a result, the theoretical thickness (h_{ox}) of normal PAMs (both thick and thin) is expected to follow the integral form of $h_{ox} = k \int_0^t i dt$ with k a constant. The solid curve in Fig. 4(a) is the theoretical relationship between the nanopore thickness ($h_{ox} - d_2$) and the anodization time, based on the typical current–time characteristics of the second anodization shown in Fig. 4(b). For comparison, we have also presented the thickness data obtained directly from the SEM images

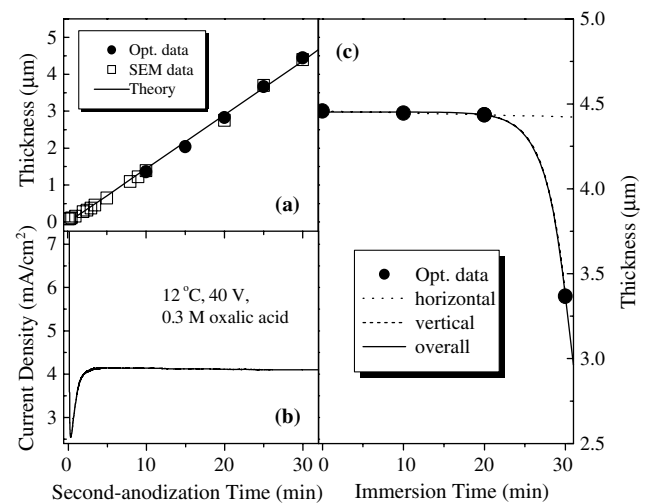


Fig. 4. (a) Nanopore thickness d_1 in the as-prepared PAMs with different second-anodization times. (b) Typical current density–time characteristics of the second anodization. (c) Nanopore thickness d_1 of the PAMs under different immersion times from 0 (as prepared) to 30 min with the same second-anodization time of 30 min.

of PAMs with T_a from 4 s to 30 min (open squares). It is clear that the yielded PAM thickness from the optical analysis is in good agreement with both the FE-SEM data and the theoretical expectation from the current density-anodization time characteristics.

The filled circles in Fig. 4(c) are the calculated optical thickness of the PAMs under different immersion times from 0 (as prepared) to 30 min with the same second-anodization time of 30 min. It is expected from the interference fringes that we can observe a rapid decrease in the thickness at the immersion time longer than 20 min. As we know, the dissolution of alumina occurs both horizontally and vertically to the nanopores with the same dissolution speed when the PAMs are immersed in the 5 wt% phosphoric acid. Our dissolution test for the barrier layers in 5 wt% phosphoric acid reveals that the dissolution rate is approximately 1.3 nm/min. However, due to the large difference between the nanopore thickness (in μm) and the nanopore diameters ($\sim 40 \text{ nm}$), inhomogenous dissolution exists in each column of the nanopore arrays [17]. The dissolution rate decreases with the increase of the depth in each nanopore column, since the phosphoric acid is thought to circulate more effectively near the surface than deep in the pores.

For the horizontal dissolution to the nanopores, the reduction of the nanopore thickness will have the rate of $\sim 1.3 \text{ nm/min}$, as shown the dotted curve in Fig. 4(c). Nevertheless, in the case of vertical dissolution, it will take about 23 min to dissolve the surface part of the $\sim 60 \text{ nm}$ diameter alumina sidewalls from both sides. As a result, more and more alumina sidewalls will be dissolved vertically, and an exponential decrease in the nanopore thickness is expected after the immersion time of $\sim 23 \text{ min}$. The dashed curve in Fig. 4(c) presents the dramatic reduction of the nanopore thickness due to the vertical dissolution by $d_1 = 4.45 - 0.0166 \cdot \exp[(T_i - 20)/2.4]$ (in μm). The yielded overall variation of nanopore thickness (solid curve) due to both the horizontal and vertical dissolution can well explain the experimental observation. It is clear that the vertical dissolution plays a key role in the nanopore thickness reduction. The fitted barrier layer thickness d_2 is found to be $40 \pm 1 \text{ nm}$ (the same as the SEM results) in the as-prepared PAMs, and decreases at a rate of $0.25 \pm 0.05 \text{ nm/min}$ in 5 wt% phosphoric acid.

In addition to the thickness, the refractive index of PAMs can also be extracted from the transmission model simultaneously. It should be noted that the effective refractive index of PAMs differs from the refractive index n_1 of the host alumina, and varies with porosity as well as the refractive index n_2 of a guest material in the pores. In our present work, n_2 is considered to be 1 as air is the guest material. Fig. 5 shows the yielded wavelength-dependent refractive index n_1 of the host alumina in PAMs under different immersion times (0–30 min) with the second-anodization time from 10 to

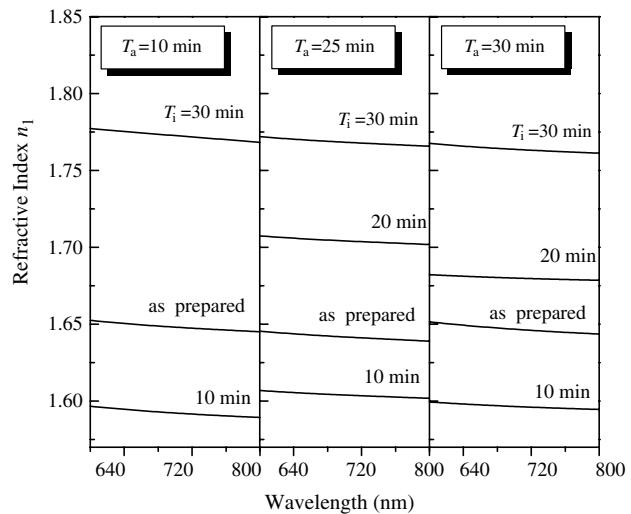


Fig. 5. Yielded wavelength-dependent refractive index n_1 of the host alumina in the PAMs under different second-anodization times $T_a = 10, 25$, and 30 min with the immersion times $T_i = 0, 10, 20$ and 30 min , respectively.

30 min. The refractive index n_1 of the host alumina in as-prepared PAMs is calculated to be about 1.65 at 600 nm, which is consistent with the reported values obtained by optical waveguide method [25]. We note that the refractive index n_1 does not change dramatically with the wavelength. Nevertheless, the refractive index changes rapidly with the immersion time, i.e., first decreases and then increases with the immersion time.

Considering that the anion-incorporated alumina has low dielectric constants [21], we suggest that this kind of nonmonotonic $n_1(T_i)$ behavior can be explained by the nonuniform distribution of anions in the host alumina. It has been reported that the oxalic impurities can replace O^{2-} in the oxide as substitution or contamination impurities within some depth in the outer oxide layer of host alumina [26–28], and the inner oxide layer consists of pure alumina with the thickness of about 9 nm [23]. Similar to the PO_4^{3-} in phosphoric acid anodized alumina [21], the mobility of oxalic anions $\text{C}_2\text{O}_4^{2-}$ is responsible for the nonuniform anion concentration. The absorbed $\text{C}_2\text{O}_4^{2-}$ moving towards the anode during anodization is delayed in the intermediate part of outer oxide layer, because of its larger size and lower mobility than OH^- and O^{2-} . As a result, $\text{C}_2\text{O}_4^{2-}$ concentrates in the intermediate part of the outer wall, and in this region the lower refractive index of host alumina can be observed, approximately at $T_i = 10 \text{ min}$. As the immersion goes on, the dissolution vertical to the nanopores is expected to reach the inner oxide of pure alumina and a high refractive index of ~ 1.77 at 600 nm is observed under $T_i = 30 \text{ min}$, in good agreement with the generally reported data [18]. From Fig. 5, we also observe the trivial effects of the second-anodization time T_a on the refractive index.

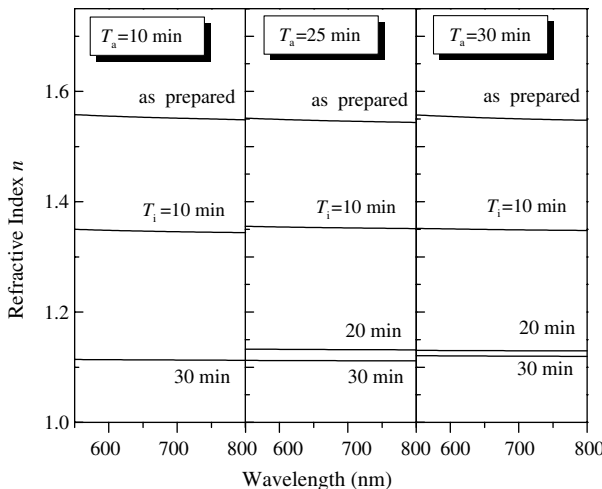


Fig. 6. Yielded wavelength-dependent refractive index n of the highly ordered nanopore arrays in the PAMs under different second-anodization times $T_a = 10, 25$, and 30 min with the immersion times $T_i = 0, 10, 20$ and 30 min, respectively.

Fig. 6 displays the wavelength-dependent refractive index n of the highly ordered nanopore arrays, which is calculated according to the Bruggeman's effective medium approximation (BEMA) model [29] with the obtained refractive index n_1 of the host alumina:

$$\left\{ \begin{array}{l} \sum_{i=1}^2 f_i \frac{\varepsilon_i - \varepsilon}{\varepsilon_i + 2\varepsilon} = 0, \\ \sum_{i=1}^2 f_i = 1, \end{array} \right. \quad (3)$$

where $\varepsilon_1 = (n_1)^2$ and $\varepsilon_2 = 1$ are the dielectric constants of the host alumina and air, respectively, and f_i denotes their respective volume fraction, which is obtained from the values of porosity. The reason why we have adopted the BEMA to analyze the role of the nanopore arrays is that BEMA has been widely used to calculate the corresponding effective dielectric function of a mixture medium containing nanoscale voids [29]. The yielded results are naturally considered to be the average ones. From Fig. 6, the effective refractive index n is found to decrease with the increase of porosity (immersion time), as expected. The highest refractive index of the as-prepared PAMs is about 1.55 with a porosity of 0.145, which is again consistent with the result obtained by optical waveguide method [25].

Finally, we discuss the band gaps and band tails of the PAMs, which can be obtained by calculating the optical transmission spectra in the ultraviolet range (Figs. 2(b) and 3(b)) through the sigmoidal equation of the absorption coefficient $\alpha(E)$ [30]

$$\alpha(E) = \frac{\alpha_0}{[1 + \exp\left(\frac{(E_g - E)}{\Delta E}\right)]} \quad (4)$$

with α_0 a fitting parameter, E_g the “effective” band gap, and ΔE the Urbach broadening factor. The solid curves

in Figs. 2(b) and 3(b) are the calculated transmission edges, taking into account the interface reflection and optical scattering losses in the transmission spectra. The effective band gaps and band tails of these PAMs have been evaluated to be ~ 4.2 eV and ~ 0.15 eV, respectively, and do not change much (within 0.1 eV for band gaps and 0.02 eV for band tails) with the PAM porosities and thicknesses.

It is generally accepted that the true effective optical gap lies in the vicinity of the rising edge of the transmission spectra, as can be clearly observed from Figs. 2 and 3. Therefore, the effective optical band gaps E_g of ~ 4.2 eV are justified, though the yielded values in these oxalic-produced PAMs are much smaller than the bulk γ -Al₂O₃ band gap of 8.7 eV [31]. In fact, the observed effective band gaps in PAMs can be attributed to the interband transition from valence band to unoccupied states located in the band gaps [32]. These unoccupied states are expected to be induced by defects [31] in these oxalic-produced PAMs. By assuming the existence of ideal vacancies in alumina, Ciraci and Batra [33] have theoretically obtained empty energy levels located in the band gaps under the density of states calculation. The experimental PL spectra [16] and X-band electron paramagnetic resonance results [14] have also demonstrated the existence of oxygen vacancies (F^+ centers) and oxalic impurities in the PAMs, which may contribute to the empty energy levels in the band gaps.

4. Conclusions

We have employed the optical transmission measurements for the study of optical properties in highly ordered oxalic-produced PAMs with different thicknesses (induced by different second-anodization times) and porosities (induced by different phosphoric acid immersion times). The calculated optical thickness as a function of second-anodization time agrees well with the FE-SEM data and the theoretical results from the current density-time characteristics. Based on the yielded PAM thickness under different immersion times, we propose the inhomogeneous dissolution process of alumina in phosphoric acid. It is found that the wavelength-dependent refractive index of the host alumina shows a nonmonotonic behavior with the immersion time due to the nonuniform distribution of impurities in the outer oxide layer. Based on the calculated refractive index of host alumina, the effective refractive index of nanopores array without barrier layer can be easily estimated through BEMA. In comparison with the bulk alumina, the reduction of band gaps and appearance of band tails in PAMs are attributed to the existence of unoccupied defect states in the band gaps, which may originate from the oxygen vacancies (F^+ centers) and oxalic impurities in the PAMs. The optical trans-

mission measurement is thus demonstrated to be an effective way for optical investigation of the highly ordered PAMs.

Acknowledgments

This work was supported by the Natural Science Foundation of China under contract No. 10125416, the Shanghai Major Project of 03DJ14003, and the Shanghai Nanotechnology Fundamental Research Project of 0352nm013.

References

- [1] H. Masuda, K. Fukuda, *Science* 268 (1995) 1466.
- [2] X. Mei, D. Kim, H.E. Ruda, Q.X. Guo, *Appl. Phys. Lett.* 81 (2002) 361.
- [3] P.R. Evans, G. Yi, W. Schwarzacher, *Appl. Phys. Lett.* 76 (2000) 481.
- [4] K. Nielsch, F. Müller, A.-P. Li, U. Gösele, *Adv. Mater. (Weinheim, Ger.)* 12 (2000) 582.
- [5] M.J. Zheng, L.D. Zhang, G.H. Li, X.Y. Zhang, X.F. Wang, *Appl. Phys. Lett.* 79 (2001) 839.
- [6] J.S. Suh, J.S. Lee, *Appl. Phys. Lett.* 75 (1999) 2047.
- [7] J. Liang, S.-K. Hong, N. Kouklis, R. Beresford, J.M. Xu, *Appl. Phys. Lett.* 83 (2003) 1752.
- [8] G. Che, B.B. Lakshmi, E.R. Fisher, C.R. Martin, *Nature (London)* 393 (1998) 346.
- [9] G. Sauer, G. Brehm, S. Schneider, K. Nielsch, R.B. Wehrspohn, J. Choi, H. Hofmeister, U. Gösele, *J. Appl. Phys.* 91 (2002) 3243.
- [10] K. Nielsch, R.B. Wehrspohn, J. Barthel, J. Kirschner, U. Gösele, S.F. Fischer, H. Kronmüller, *Appl. Phys. Lett.* 79 (2001) 1360.
- [11] R. Karmhag, T. Tesfamichael, E. Wäckelgård, G.A. Niklasson, M. Nygren, *Sol. Energy* 68 (2000) 329.
- [12] H. Masuda, M. Ohya, H. Asoh, M. Nakao, M. Nohtomi, T. Tamamura, *Jpn. J. Appl. Phys.* 38 (1999) L1403.
- [13] Y. Du, W.L. Cai, C.M. Mo, J. Chen, L.D. Zhang, X.G. Zhu, *Appl. Phys. Lett.* 74 (1999) 2951.
- [14] Y. Li, G.H. Li, G.W. Meng, L.D. Zhang, F. Philipp, *J. Phys.: Condens. Matter* 13 (2001) 2691.
- [15] T. Gao, G.W. Meng, L.D. Zhang, *J. Phys.: Condens. Matter* 15 (2003) 2071.
- [16] W.L. Xu, M.J. Zheng, S. Wu, W.Z. Shen, *Appl. Phys. Lett.* 85 (2004) 4364.
- [17] L. Huang, M. Saito, M. Miyagi, K. Wada, *Appl. Opt.* 32 (1993) 2039.
- [18] S. Nakamura, M. Saito, L. Huang, M. Miyagi, K. Wada, *Jpn. J. Appl. Phys.* 31 (1992) 3589.
- [19] M. Saito, M. Kumagai, M. Miyagi, K. Wada, *Appl. Opt.* 30 (1991) 2257.
- [20] J. Hohlbein, U. Rehn, R.B. Wehrspohn, *Phys. Status Solidi (a)* 201 (2004) 803.
- [21] J. Choi, Y. Luo, R.B. Wehrspohn, R. Hillebrand, J. Schilling, U. Gösele, *J. Appl. Phys.* 94 (2003) 4757.
- [22] H. Chen, M.H. Gullanar, W.Z. Shen, *J. Cryst. Growth* 260 (2004) 91.
- [23] K. Nielsch, J. Choi, K. Schwirn, R.B. Wehrspohn, U. Gösele, *Nano Lett.* 2 (2002) 677.
- [24] G. Patermarakis, K. Moussoutzanis, *Electrochim. Acta* 40 (1995) 699.
- [25] M. Saito, M. Shibasaki, S. Nakamura, M. Miyagi, *Opt. Lett.* 19 (1994) 710.
- [26] Y. Yamamoto, N. Baba, S. Tajima, *Nature (London)* 289 (1981) 572.
- [27] F.Y. Li, L. Zhang, R.M. Metzger, *Chem. Mater.* 10 (1998) 2470.
- [28] G.E. Thompson, G.C. Wood, *Nature (London)* 290 (1981) 230.
- [29] T.D. Kang, H. Lee, S.J. Park, J. Jang, S. Lee, *J. Appl. Phys.* 92 (2002) 2467.
- [30] H.P. Zhou, W.Z. Shen, N.B. Chen, H.Z. Wu, *Appl. Phys. Lett.* 85 (2004) 3723.
- [31] I. Costina, R. Franchy, *Appl. Phys. Lett.* 78 (2001) 4139.
- [32] B. Ealet, M.H. Elyakhloufi, E. Gillet, M. Ricci, *Thin Solid Films* 250 (1994) 92.
- [33] S. Ciraci, I.P. Batra, *Phys. Rev. B* 28 (1983) 982.